Materials Science & Engineering A 648 (2015) 243–251

Contents lists available at ScienceDirect

Materials Science & Engineering A

journal homepage: www.elsevier.com/locate/msea

Size effect and boundary type on the strengthening of nanoscale domains in pure nickel

Fuping Yuan*, Xiaolei Wu

State Key Laboratory of Nonlinear Mechanics, Institute of Mechanics, Chinese Academy of Science, No.15, North 4th Ring, West Road, Beijing 100190, People's Republic of China

ARTICLE INFO

Article history:
Received 1 July 2015
Received in revised form
14 September 2015
Accepted 15 September 2015

Keywords:
Dislocation
Orowan's strengthening
Molecular dynamics
Pinning strength
Nano-domains

ABSTRACT

A series of large-scale molecular dynamics simulations were carried out to investigate the interactions between an extended edge dislocation ($1/2<112>\{111\}$) and nanoscale domains in pure nickel. The pinning strength of nano-domains and the corresponding atomistic interaction mechanisms were found to be closely related to the domain boundary type, the domain size and spacing. The pinning strengths were found to be higher for high-angle domains than those for low-angle domains at the same size scale, and increase with increasing domain size and decreasing domain spacing. Unlike the by-pass via interactions between the dislocation and boundaries for high-angle domains (much like the role of hard precipitates in alloys), the dislocation was found to cut partly through the low-angle domains. Thus the dragging force from the boundary segments of the low-angle domains should be smaller when compared to the Orowan's strengthening for "hard particles", such as high-angle domains. The predictions from Ashby's model on Orowan's strengthening are higher than the simulation data for low-angle domains, while agree relatively well with those for high-angle domains. Moreover, a more universal model was proposed to connect the dislocation line shape at the critical shear strain with the pinning strength.

1. Introduction

Superior strength–ductility synergy has always been the pursuit of materials scientists and engineers for structural applications. However, this is not a easy task since strength and ductility are mutually exclusive in general [1–7]. Due to the well-known Hall–Petch effect of grain boundary (GB) strengthening, the yield strength of ultrafine-grained (UFG) and nanocrystalline (NC) metals can be enhanced several times over that of coarse-grained (CG) counterpart [3,5–7], however their uniform tensile elongations are typically low. This is because dislocations are readily annihilated by abundant GBs, and dislocation interactions and storage of dislocations become difficult in grain interior due to the limited room by structural refinement [7,8]. Several strategies with microstructures at the nanoscale have been attempted to evade such strength–ductility dilemma recently, such as, bimodal grain size distribution, engineering coherent twin boundaries (TBs) at the nanoscale, nano-precipitate dispersion and gradient nano-grained structure [1,9–19].

A defect engineering strategy to resolve such strength–ductility trade-off paradox in pure nickel was described in our recent work [20], where a yield strength of ~1.3 GPa together with a uniform tensile elongation of ~27% was observed. Thus, a dream combination from two extreme worlds was achieved in the nano-domained Ni: not only as strong as nanocrystalline Ni but also as ductile as coarse-grained Ni. Spread-out distributions of nanoscale domains (ranging from 3 to 12 nm in size) with the volume fraction of only a few % were architected inside the UFG pure Ni grains by a pulsed electrodeposition procedure [20]. The pre-planted nano-domains can play dual roles: on one hand, nano-domains block dislocations effectively, just like precipitates for Orowan strengthening in alloys [21–23]; on the other hand, with ample space in the grain interior due to the low volume fraction of nano-domains, the domain boundaries can also be effective dislocation sources and trapping sites of running dislocations for efficient dislocation multiplication and storage in the grain interior, resulting in a pronounced strain hardening rate to sustain large uniform elongations.

Large-scale molecular dynamics (MD) simulations have proven to be particularly useful and been widely used to investigate details of atomistic interaction mechanisms between dislocations and various types of defects, such as voids, precipitates and Guinier–Preston (GP) zone in different metal and alloys [24–34]. In such simulations, the motion of a dislocation can be driven by applying shear strain or stress on the surfaces of the MD simulation units, and the critical resolved shear stress (CRSS) for unpinning can be easily calculated [30–32]. These studies indicated that

* Corresponding author. Fax: +86 10 82543977.

http://dx.doi.org/10.1016/j.msea.2015.09.071
0921-5093/

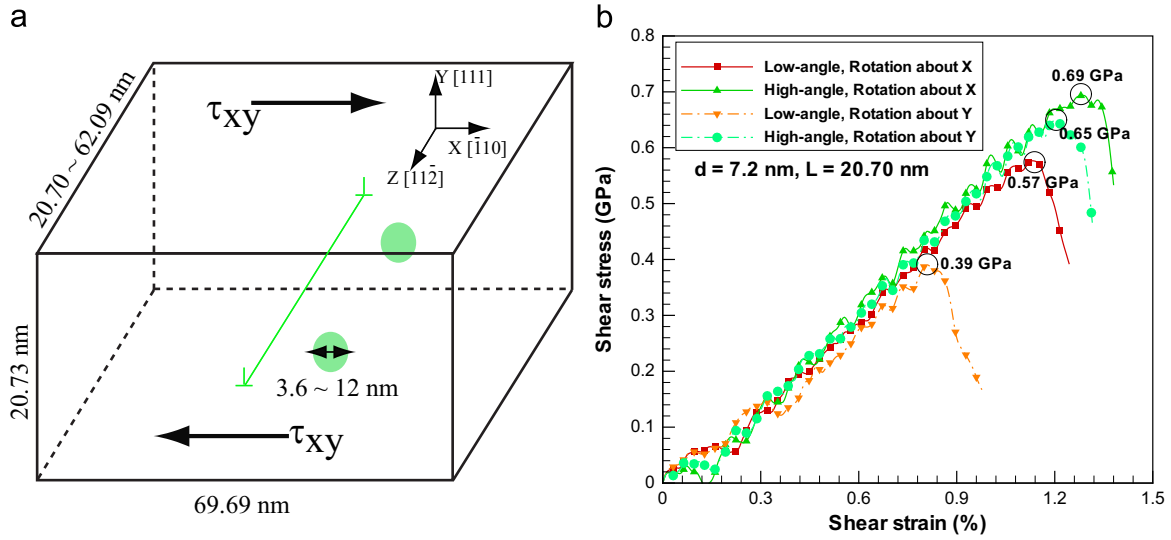

Fig. 1. (a) Configuration for simulation cell with a straight edge dislocation and two nano-domains; (b) Simulated shear stress–shear strain curves for four different configurations with low-angle/high-angle domains and various orientations (d=7.2 nm, L=20.70 nm). (For interpretation of the references to color in this figure, the reader is referred to the web version of this article.)

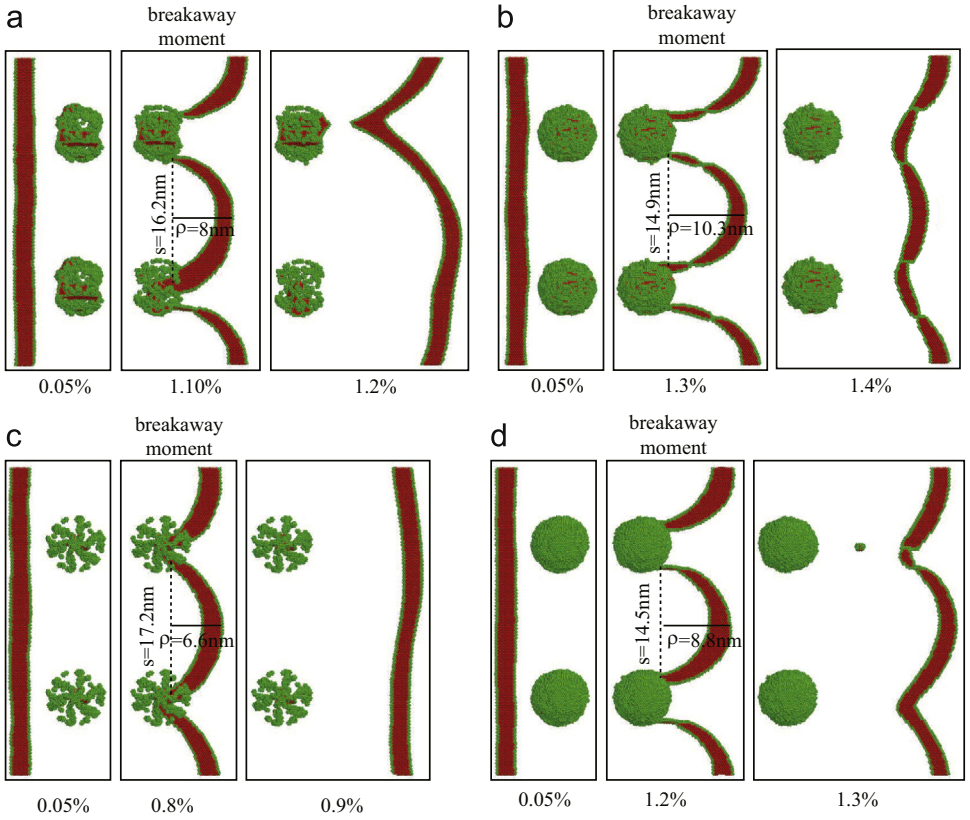

Fig. 2. A sequence of snapshots at different shear strains showing the pinning of the dislocation, its interaction with the nano-domains and its subsequent breakaway: (a) low-angle nano-domains (6°) rotated about the X axis; (b) high-angle nano-domains (90°) rotated about the X axis; (c) low-angle nano-domains (6°) rotated about the Y axis; (d) high-angle nano-domains (90°) rotated about the Y axis.

the interactions can be very complex due to the variety of interacting mechanism, and the CRSS was found to be size-dependent [24–34]. In our previous reported heterogeneously architected Ni with nanoscale domains [20], the domain size was varied from 3 to 12 nm and the domain spacing was varied from several nm to tens of nm although an average domain size of ~7 nm and an average domain spacing of ~20 nm were realized. Although most of domain boundaries were low-angle boundaries ($<15°$), a small fraction of high-angle domain boundaries also exist. There is clearly a lack of understanding of the effects of the domain boundary type, the domain size and spacing on the atomistic interaction mechanisms with dislocations. In this regard, a series of large-scale MD simulations were carried out in the present study to investigate dislocation-domain interactions in Ni, focusing on the effects of several factors mentioned above on the pinning strength and the dislocation line shape at the critical shear strain.

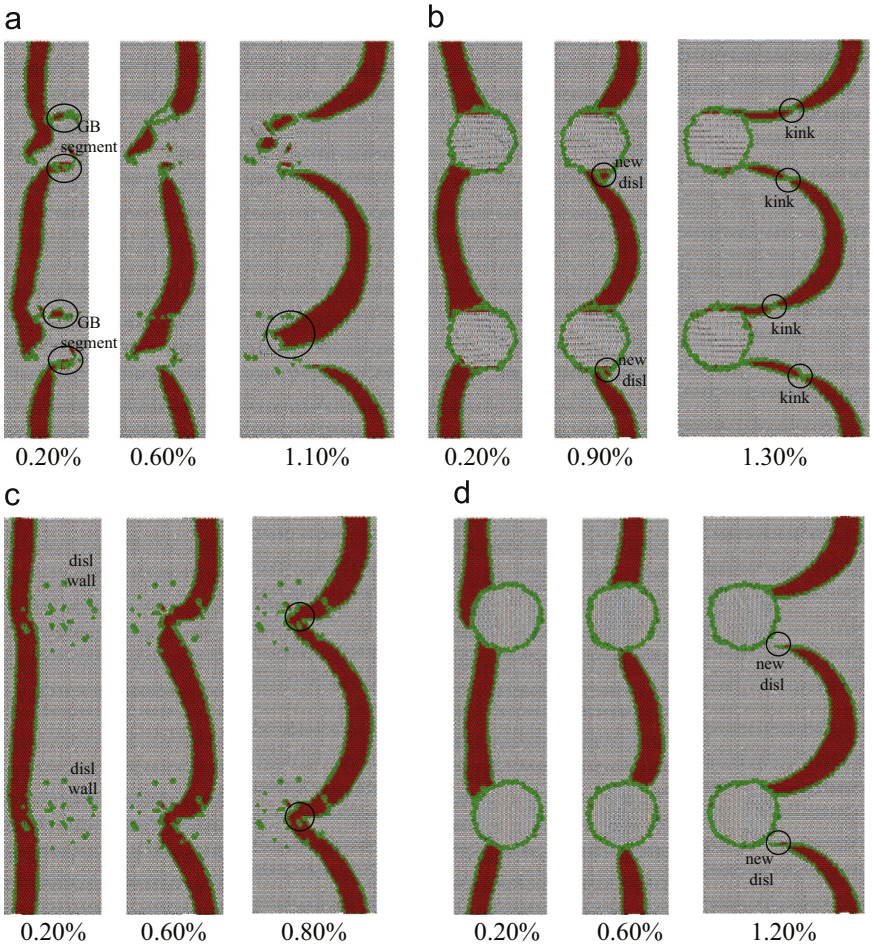

Fig. 3. A sequence of snapshots of thin slices at different shear strains showing the details of interactions between the dislocation and nano-domain: (a) low-angle nano-domains (6°) rotated about the *X* axis; (b) high-angle nano-domains (90°) rotated about the *X* axis; (c) low-angle nano-domains (6°) rotated about the *Y* axis; (d) high-angle nano-domains (90°) rotated about the *Y* axis.

2. Simulation techniques

The MD simulations were performed using the Large-scale Atomic/Molecular Massively Parallel Simulator (LAMMPS) code. The force calculations between atoms were achieved by a Ni EAM potential developed by Mishin et al. [35]. In order to study the interaction of a straight edge dislocation with nano-domains, the simulation cells (Fig. 1a) with a perfect fcc Ni lattice, bounded by ($[\bar{1}10]$), ($[111]$) and ($[11\bar{2}]$) faces in the *X*, *Y* and *Z* directions respectively, were first constructed. An edge dislocation with the burgers vector of $\vec{b} = 1/2[\bar{1}10]$, was created in the center of the simulation cells ($X=Y=0$), with the line direction parallel to the *Z* axis, using the continuum displacement field [31]. Then the nano-domains were created by rotating the corresponding spherical domains with respect to their equators about *X* or *Y* axis for 6° (low-angle domains) or 90° (high-angle domains). Two nano-domains with diameters of 3.6–12 nm were created in each cell separated by distances of 10.35–31.04 nm (half length along *Z* axis). The cell size was $69.69 \times 20.73 \times 62.09$ nm^3 and contained roughly 8.3 million atoms for domain spacing of 31.04 nm. Periodic boundary condition was imposed in the *Z* direction, while *X* direction was set to be free boundary condition. The cells were divided into three regions in *Y* direction, consisting of a freely mobile section and two thin rigid blocks (upper and downer, wherein the atoms were fixed in their positions) as boundary planes for applying shear displacement. Prior to shear loading, the as-created samples were first subjected to energy minimization by the conjugate gradient method, then the Nose/Hoover isobaric–isothermal ensemble (NPT) was performed for 100 ps to finally relax the samples under both the pressure 0 bar (along the *Z* direction) and the desired temperature (1 K). After relaxation, the cells were then loaded in shear by subjecting the atoms in the upper and downer rigid blocks to a constant velocity in the *X* direction, giving a shearing strain rate of 1×10^8/s and driving the dislocation for movement toward nano-domains. In all cases, nano-domains were positioned so that the slip plane of the dislocation would intersect their centers. In order to visualize the interacting sequences, common neighbor analysis (CNA) was used. Gray color is for perfect fcc atoms, red color is for hcp atoms and green color is for GBs, dislocation core, free surface and other atoms [36].

3. Results and discussions

3.1. Effect of domain boundary type on the strengthening

When considering the effect of domain boundary type, the domain size and spacing were fixed at 7.2 nm and 20.7 nm, respectively. Four different domain boundary types were considered here, i.e., low-angle boundary rotated about *X* axis (type I), high-angle boundary rotated about *X* axis (type II), low-angle boundary rotated about *Y* axis (type III) and high-angle boundary rotated about *Y* axis (type IV). One of {111} planes for the domains is consistent with the slip plane of the edge dislocation when

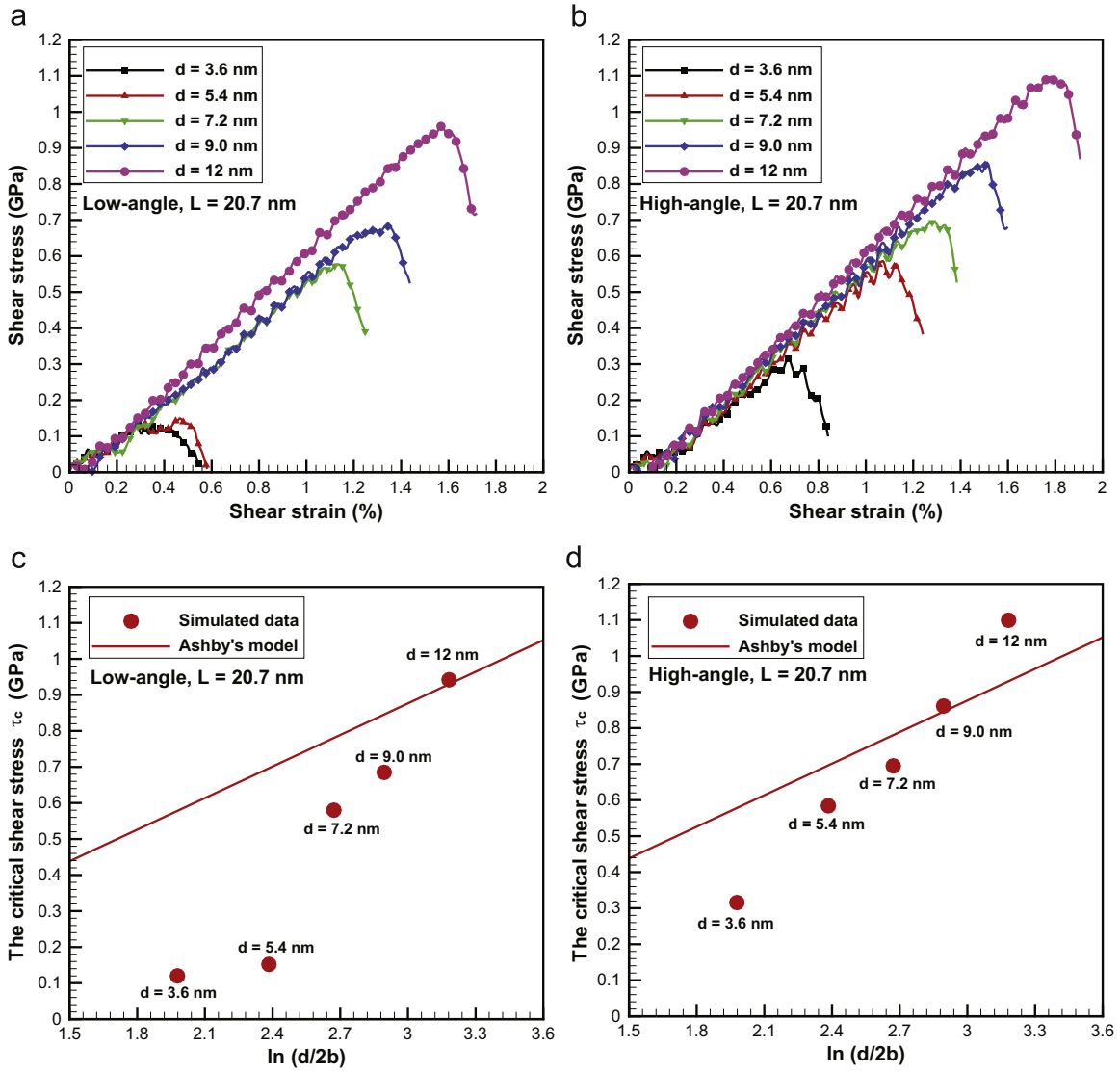

Fig. 4. Simulated shear stress–shear strain curves for different configurations with fixed L (L=20.7 nm) and various d: (a) low-angle domains; (b) high-angle domains. The critical shear stress versus ln(d/2b), and the prediction of Ashby's model [21] is drawn by the full straight line: (c) low-angle domains; (d) high-angle domains.

rotating about Y axis, while all {111} planes for the domains are different from the slip plane of the edge dislocation when rotating about X axis. The shear stress and shear strain could be calculated by the following equations:

$$\tau_{xy} = \frac{f_{rigid}}{A} \tag{1}$$

$$\gamma = \frac{|t_{upper}| + |t_{downer}|}{h_{mobile}} \tag{2}$$

where f_{rigid} is the average force acting on the upper/downer rigid blocks in the X direction, A is the surface area of the upper/downer rigid block, t_{upper} and t_{downer} are the displacements of the upper and downer rigid blocks respectively, h_{mobile} is the height of the mobile block along the Y direction.

Simulated shear stress–shear strain curves for four different domain boundary types during the interaction of the dislocation with nano-domains are presented in Fig. 1b. The shear stress is observed to increase first with increasing shear strain due to the strengthening effect of nano-domains for dislocation motion, reach a peak at the critical shear strain for unpinning moment and then drop with further shear strain attributed to the release of the dislocation from nano-domains. The CRSS could be obtained in Fig. 1b by the breakaway moment of the dislocation from nano-domains, identified by visualization in Fig. 2 later. It is shown that the CRSS of the high-angle domains is higher than that of the low-angle domains, and larger CRSS value is observed for the cases rotating about X axis compared to the cases rotating about Y axis.

The domain boundary type effect on the corresponding interaction sequences and the critical dislocation line shapes will be discussed here. Snapshots at different shear strains showing the pinning of the dislocation, its interactions with the nano-domains and its subsequent breakaway, are presented in Fig. 2. As indicated in the simulation details, the samples were relaxed via energy minimization and followed by relaxation under NPT ensemble before shear loading. The relaxation allows the full dislocation, which was initially created using the continuum analytic displacement field, to relax into two partial dislocations separated by a stacking fault with a distance of about 2 nm (Fig. 2). When the shear strain was applied, the following interaction sequences were revealed: (i) the dislocation initially glides toward the nano-domains; (ii) the dislocation interacts with the nano-domains and is

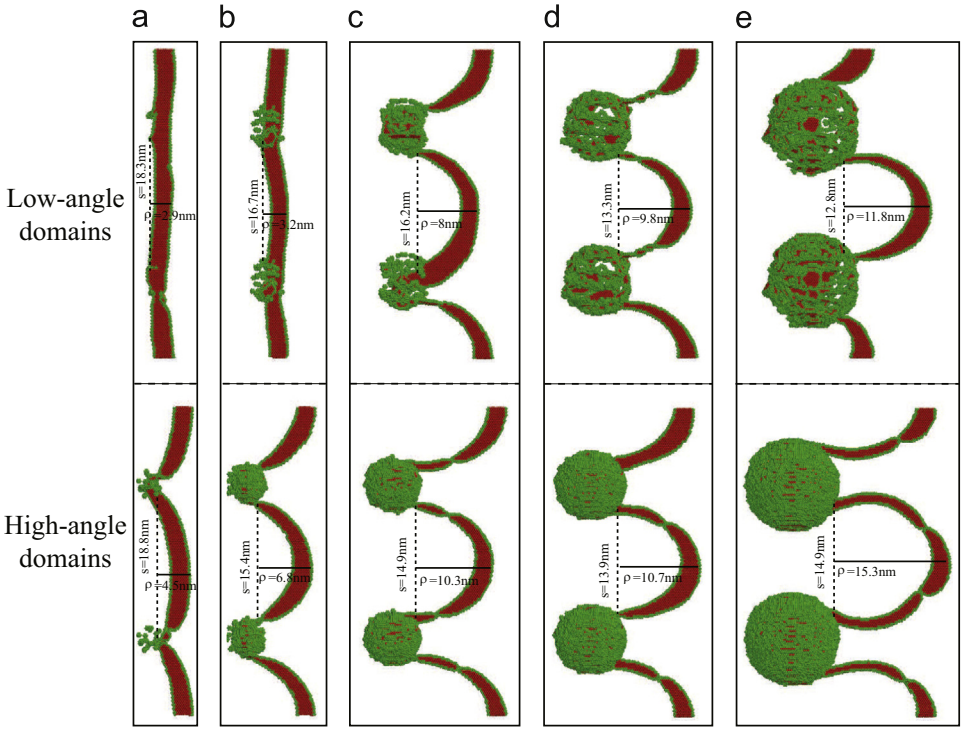

Fig. 5. The simulated configurations at the critical shear strain showing the breakaway curvature for different configurations with fixed L (L=20.7 nm) and various d: (a) d=3.6 nm; (b) d=5.4 nm; (c) d=7.2 nm; (d) d=9 nm; (e) d=12 nm.

pinned by the nano-domains; (iii) the nano-domains force the incident dislocation line to bow in between them; (iv) finally, the breakaway of the dislocation happens when the applied shear stress reaches the CRSS. At the breakaway moment, the domain boundary type is found to have a strong influence on the curvature of the dislocation line (Fig. 2), which could be considered as the pinning ability of the nano-domains. The curvature of the dislocation line could be described by the bowing parameter of ρ/s, where ρ is the bulging in distance and s is the width for two pinned arms. The bowing parameter (ρ/s) of the high-angle domains is found to be higher than that of the low-angle domains, and larger value of ρ/s is observed when rotating about X axis compared to Y axis. This is consistent with the influence of the domain boundary type on the CRSS, as shown in Fig. 1a.

Thin slices along the Y direction (-0.3 nm $< Y <$ 0.3 nm) were used in order to show the details for the domain boundary type effects on the atomistic interaction and pinning mechanisms. Then snapshots with thin slices at different shear strains are presented in Fig. 3. Since the misorientation angle is small (6°) for the low-angle domains rotated about the X axis (type I), the boundaries are split into several boundary segments and discontinuous. Thus the incoming dislocation can only be pinned by the boundary segments, and some part of the incoming dislocation can cut into the nano-domains once the incoming dislocation hits the nano-domains of type I. In this regard, as compared to the Orowan's strengthening for "hard particles" [21,29,32], the dragging force and the pinning strength from the boundary segments should be smaller. For the low-angle domains rotated about the Y axis (type III), the boundaries are actually dislocation walls consisting a group of dislocations. Since the slip plane of the edge dislocation is also one of {111} planes for the domains of type III, the dislocation can almost cut into the nano-domains when hitting them and is only dragged by several dislocations in the dislocation walls, resulting in an even smaller pinning strength when compared to the domains of type I. When the dislocation hits the high-angle nano-domains (type II and type IV), different from the cases of the low-angle nano-domains (type I and type III), the incoming dislocation deposits itself along and interacts with the boundary surfaces of nano-domains. This interaction mechanism is qualitatively similar to Orowan looping for "hard particles" [21], which should require higher CRSS values and pinning strength compared to the low-angle domains (type I and type III). Moreover, the CRSS is observed to be higher in the nano-domains of type II than in the nano-domains of type IV since the slip plane of the edge dislocation is also one of {111} planes for the domains of type IV, which resulting in lower dragging force for type IV. As shown in Fig. 3b and d, new dislocations are also observed to nucleate from the boundary surfaces of nano-domains (type II and type IV), which creates kinks in the arms of the curved dislocation during the interacting process. This kink formation should also result in higher CRSS values and pinning strength for dragging the dislocation.

3.2. *Effects of the domain size and spacing on the strengthening*

When considering the effects of domain size and spacing, the domain boundary types were all rotated about the X axis. First, the effect of domain size on low-angle nano-domains and high-angle nano-domains were considered, and the domain spacing was fixed at 20.7 nm. Fig. 4a and b shows the simulated shear stress–shear strain curves for different nano-domains with various domain sizes (d). The CRSS can be obtained from these curves, and then the influences of the domain size on the CRSS are plotted in Fig. 4c and d. It is observed that the CRSS increases with increasing domain size (d). In the MD simulations, Peierls stress is required to activate gliding of the dislocation before hitting the nano-domains, however the Peierls stress for our situation is very small ($<$20 MPa) and negligible compared to the CRSS values. So the CRSS values measured from Fig. 4a and 4b can be considered as the elevation in shear strength due to the nano-domain strengthening.

In alloy with "hard particles", the particles can act as strong obstacles to dislocation movements for precipitation strengthening, also so called Orowan strengthening. This strengthening is

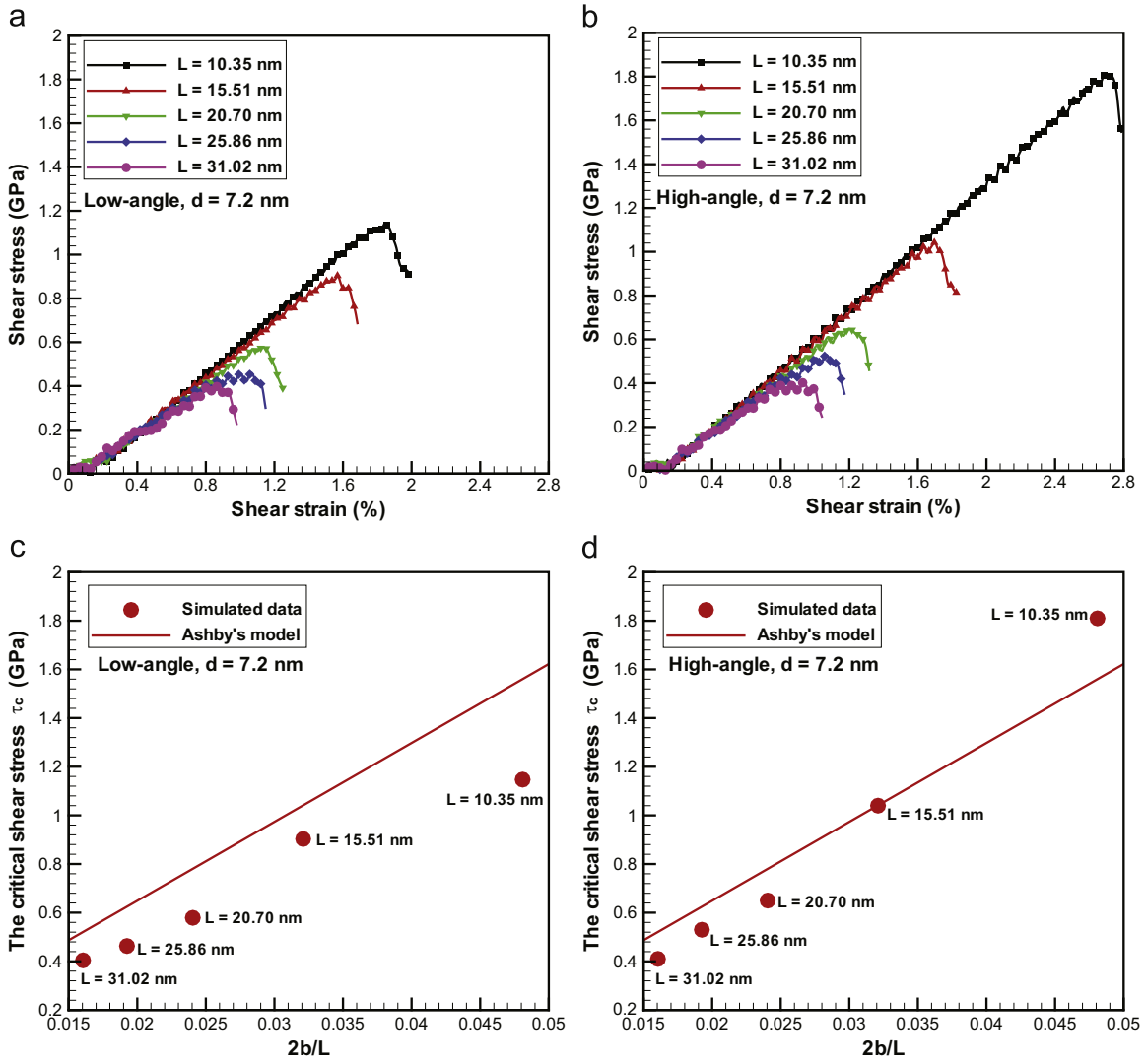

Fig. 6. Simulated shear stress–shear strain curves for different configurations with fixed d (d=7.2 nm) and various L: (a) low-angle domains; (b) high-angle domains. The critical shear stress versus $2b/L$, and the prediction of Ashby's model [21] is drawn by the full straight line: (c) low-angle domains; (d) high-angle domains.

closely related to the critical dislocation line shape when bowed around the particles, and the elevation in strength strongly depends on the average particle diameter d and the average inter-particle spacing L, and can be estimated for fine particles using Ashby's model [21],

$$\Delta\sigma = \frac{Gb}{2.38\pi(1-\nu)^{1/2}L}\ln\left(\frac{d}{2b}\right) \quad (3)$$

where G is the shear modulus (76 GPa for Ni), b is the Burgers vector (0.2489 nm for Ni), and ν is the Poisson's ratio (0.3 for Ni).

Fig. 4c and d shows the CRSS as a function of $\ln(d/2b)$, along with the predictions from Eq. (3), for low-angle domains and high-angle domains respectively. It is clearly shown that the simulation data for low-angle domains are below the predictions from Ashby's model. This is because the low-angle domains are not like second phase "hard" particles, the dislocation hitting them can partly cut into the nano-domains, attenuating the CRSS for unpinning. While the high-angle domains are "harder", and the dislocation hitting them deposits itself along the boundary surfaces and bulges in between domains without penetration. Thus, the simulation data for the high-angle domains are observed to agree much better with the predictions from Ashby's model, although the predictions are also observed to be lower than the simulation data for the high-angle domains with sizes above 9.0 nm, and higher than those for the high-angle domains with sizes below 9.0 nm.

The simulated configurations at the critical shear strain showing the breakaway curvature for different configurations with fixed L (L=20.7 nm) and various domain sizes d (low-angle domains and high-angle domains) are shown in Fig. 5. It is clearly shown that the dislocation line is severely bended under the shear stress, and the width s for two pinned arms and the bulging in distance ρ can be measured from these line shapes. The effect of domain size on the appearance of the critical dislocation line shapes is clearly indicated in Fig. 5. It is observed that the width s for two pinned arms decreases, while the bulging in distance ρ increases dramatically, with increasing domain size. Therefore, the curvature parameter ρ/s is observed to increase with increasing domain size, resulting in increasing CRSS values.

When effects of domain spacing on the CRSS and the critical dislocation line shapes were investigated, and the domain size was fixed at 7.2 nm. Fig. 6a and b shows the simulated shear stress–shear strain curves for different configurations with various domain spacing L for low-angle nano-domains and high-angle nano-domains, respectively. The CRSS is observed to increase with decreasing domain spacing L. The CRSS for the unpinning of the dislocation from the nano-domains as a function of $2b/L$ is plotted

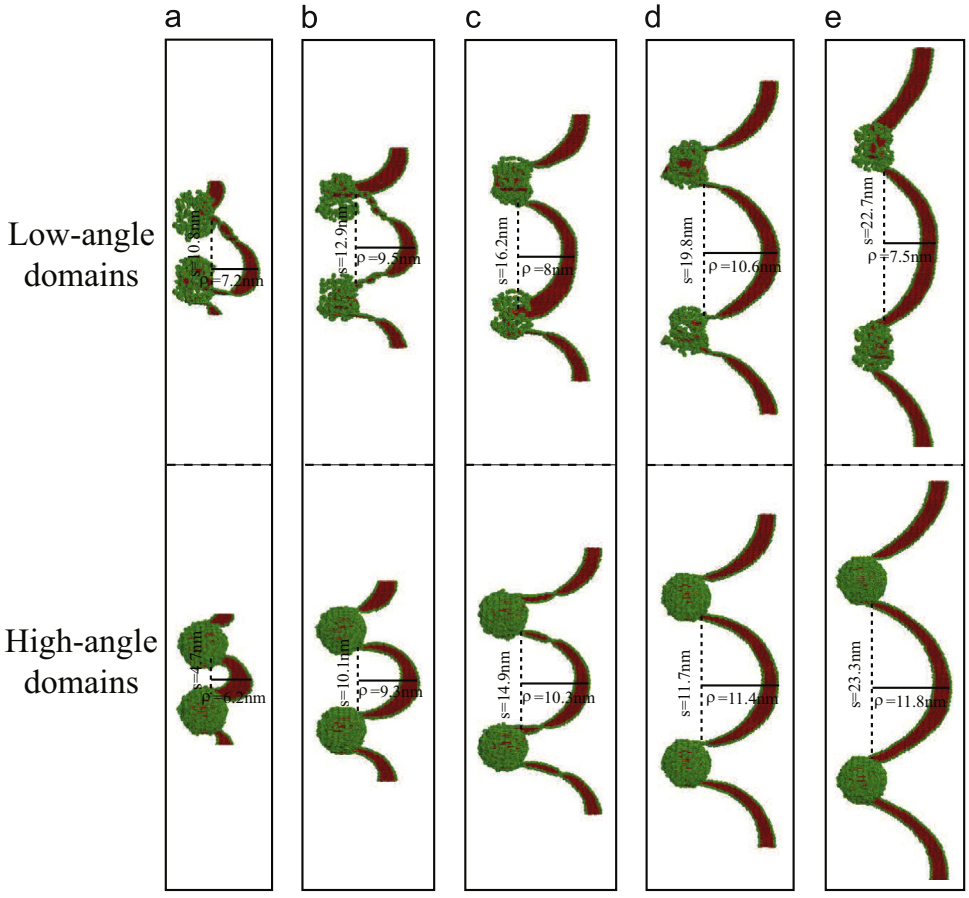

Fig. 7. The simulated configurations at the critical shear strain showing the breakaway curvature for different configurations with fixed d (d=7.2 nm) and various L: (a) L=10.35 nm; (b) L=15.51 nm; (c) L=20.7 nm; (d) L=25.86 nm; (e) L=31.02 nm.

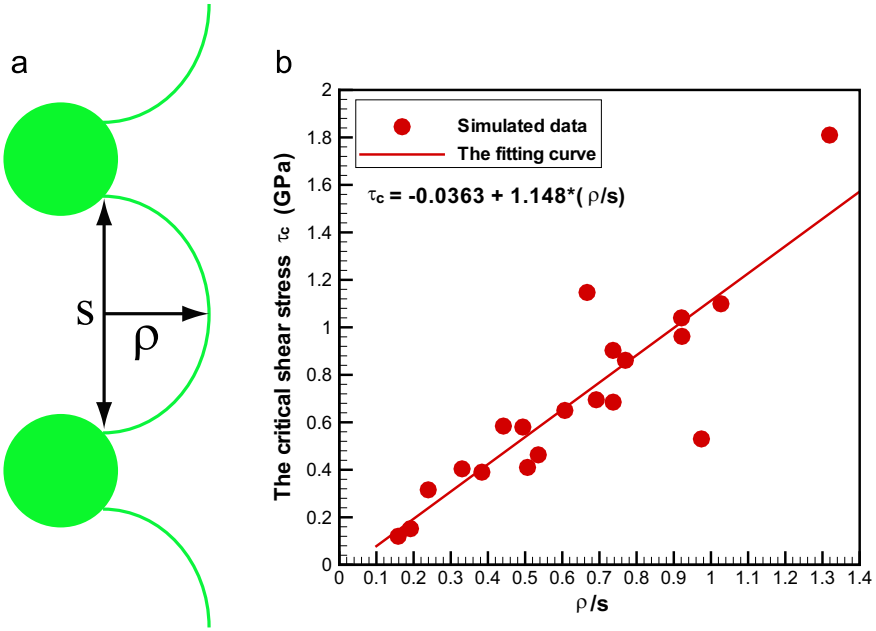

Fig. 8. (a) The typical dislocation line shape at the critical shear strain when interacting with nano-domains (the width s for two pinned arms and the bulging in parameter ρ are shown in the figure); (b) the critical shear stress versus ρ/s, and the linear fitting of simulated data is shown by the straight line.

in Fig. 6c and d, together with the predictions from Eq. (3). Again, it is shown that the simulation data for high-angle domains agree well with Ashby's model, while the simulation data for low-angle domains are much below Ashby's prediction. This is because the high-angle domains are like “hard particles” while the dislocation can partly cut into the low-angle domains.

Fig. 7 shows the simulated configurations of the critical breakaway curvatures for different configurations with fixed d (d=7.2 nm) and various L (low-angle domains and high-angle domains). The effect of domain spacing on the appearance of the

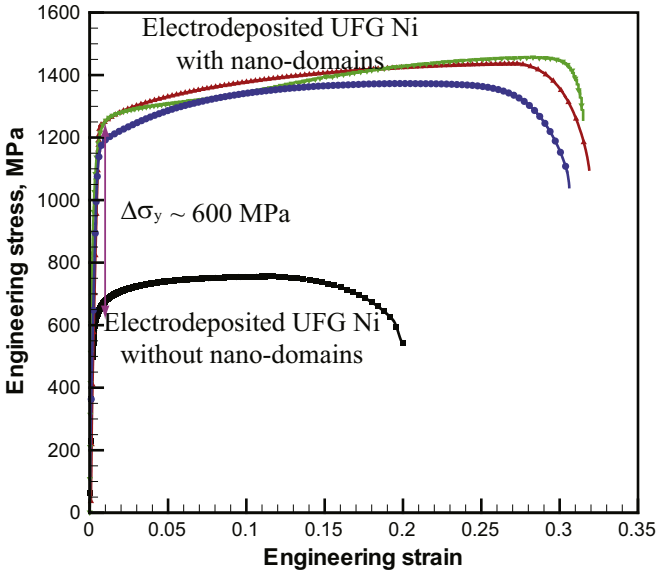

Fig. 9. Engineering stress–strain curves for the electrodeposited UFG Ni with and without nano-domains at a stain rate of $4\times10^{-4}\,s^{-1}$.

critical dislocation line shapes can be clearly analyzed in Fig. 7. The width s for two pinned arms is shown to increase dramatically and the curvature parameter ρ/s is observed to decrease with increasing domain spacing, resulting in decreasing CRSS values.

In the above discussions, it is indicated that the simulation data deviate more or less from Ashby's model, especially for the low-angle domains. However the CRSS is also indicated to be closely related to curvature parameter ρ/s at the critical line shapes, as shown in Fig. 8a. In regard of this, we propose a more universal model, which connects the dislocation line shape at the critical shear strain with the CRSS. As shown in Fig. 8b, the CRSS is linearly proportional to the curvature parameter ρ/s, regardless of domain boundary type, domain size and spacing. This can also be easily understood since the pinning strength should be directly determined by how the nano-domains can drag the dislocation, which is the exactly the critical line shape.

Fig. 9 shows the engineering stress–strain curves for the electrodeposited UFG Ni with and without nano-domains. The experiment details can be seen elsewhere [20]. The grain size of the electrodeposited UFG Ni is around 150 nm, and the domain size is varied from 3 to 12 nm (with average domain size of 7.2 nm) and the domain spacing is varied from several nm to tens of nm (with average spacing of 20.7 nm). The domain boundaries are composed of most low-angle boundaries with a small fraction of high-angle boundaries. As shown in the Fig. 9 from experiments, the uniaxial tensile yield strength elevation by the nano-domains due to the pinning effect is around 0.6 GPa, which can be converted to the shear strength elevation of ~0.35 GPa based on von Mises criterion. Our simulation results show that the CRSS for the pinning effect is varied from 0.39 to 0.69 GPa for domains with different types when taking $d=7.2$ nm, $L=20.70$ nm, as shown in Fig. 1b. It is noted that the experimental shear strength elevation (~0.35 GPa) is at the lower bound of the simulated shear strength elevations (0.39–0.69 GPa), which could be due to the high strain rate effect by the inherent limitations in MD simulations [24–34]. It also should be noted that in the real polycrystalline samples not all of incoming dislocations can overcome the nano-domains due to different orientations and Schmid factors. Some incoming lattice dislocations bulge in and get trapped between the nano-domains and entangle with the dislocations emitted from nano-domain boundaries, and even more dislocations could be generated when they interact with each other. The dislocation accumulation around nano-domains can be observed in the Bright-field TEM and HREM pictures obtained from the experiments after tensile testing in our previous paper [20], in which the dislocations with ends trapped by nano-domains can be clearly seen. Thus dislocation movements in subsequent deformation can be impeded by the accumulating dislocations in the grain volume, resulting in for enhanced strain hardening. The nano-domains thus can serve the dual purposes of (i) impeding the motion of dislocations (elevating strength) as discussed in the present study and (ii) facilitating their interaction and accumulation for increased dislocation activities (resulting in strain hardening). These dual purposes can result in a combination of extraordinary strength and ductility at the same time, setting the nano-domained nickel [20] apart from all previous (from coarse-grained all the way to nanocrystalline) nickels with a homogeneous grain structure [37–43].

4. Concluding remarks

The interaction of an extended edge dislocation ($1/2<112>\{111\}$) with nano-domains in nickel with size up to 12 nm and spacing up to 31 nm was investigated by a series of large-scale MD simulations. The key findings are summarized as follows:

(1) The CRSS of the high-angle domains was found to be higher than that of the low-angle domains, and larger CRSS value was observed when rotating about X axis instead of Y axis. the dislocations were observed to cut partly through the low-angle domains, while by-pass via interactions between the dislocations and boundaries was observed in high-angle domains.

(2) Domain size and spacing were found to have strong influences on the CRSS for breakaway of the dislocation from the nano-domains. The simulation data for high-angle domains were observed to agree relatively well with the perdictions from Ashby's model on Orowan's strengthening [21], while the perdictions were shown to be higher than those for low-angle domains.

(3) The CRSS was also found to be closely related to curvature parameter ρ/s for the critical dislocation line shapes, regardless of domain boundary type, domain size and spacing. A more universal model was also proposed to connect the dislocation line shape at the critical shear strain with the pinning strength. the present results should provide insights of tailoring defect engineering by nano-domains in metals for enhanced mechanical properties.

Acknowledgments

The authors would like to acknowledge the financial support from National Natural Science Foundation of China (Nos. 11222224, 11472286 and 11021262) and National Key Basic Research Program of China (Grants nos. 2012CB932203 and 2012CB937500). The simulations reported were performed at Supercomputing Center of Chinese Academy of Sciences.

References

[1] K. Lu, L. Lu, Science 324 (2009) 349–352.
[2] R.O. Ritchie, Nat. Mater. 10 (2011) 817–822.
[3] R.Z. Valiev, Nat. Mater. 3 (2004) 511–516.
[4] Y.T. Zhu, X.Z. Liao, Nat. Mater. 3 (2004) 351–352.
[5] R.Z. Valiev, I.V. Alexandrova, Y.T. Zhu, T.C. Lowe, J. Mater. Res. 17 (2002) 5–8.
[6] M. Dao, L. Lu, R.J. Asaro, J.T.M. de Hosson, E. Ma, Acta Mater. 55 (2007) 4041–4065.

[7] M.A. Meyers, A. Mishra, D.J. Benson, Prog. Mater. Sci. 51 (2006) 427–556.
[8] Y.M. Wang, E. Ma, Acta Mater. 52 (2004) 1699–1709.
[9] L. Lu, Y. Shen, X. Chen, L. Qian, K. Lu, Science 304 (2004) 422–425.
[10] L. Lu, X. Chen, X. Huang, K. Lu, Science 323 (2009) 607–610.
[11] X.Y. Li, Y.J. Wei, L. Lu, K. Lu, H.J. Gao, Nature 464 (2010) 877–880.
[12] Y.M. Wang, M.W. Chen, F.H. Zhou, E. Ma, Nature 419 (2002) 912–915.
[13] E. Ma, J. Miner. Met. Mater. Soc. 58 (2006) 49–53.
[14] S. Cheng, Y.H. Zhao, Y.T. Zhu, E. Ma, Acta Mater. 55 (2007) 5822–5832.
[15] P.V. Liddicoat, X.Z. Liao, Y.H. Zhao, Y.T. Zhu, M.Y. Murashkin, E.J. Lavernia, R. Z. Valiev, S.P. Ringer, Nat. Commun. 1 (2010) 1–7.
[16] T.H. Fang, W.L. Li, N.R. Tao, Lu K, Science 331 (2011) 1587–1590.
[17] X.L. Wu, P. Jiang, L. Chen, F.P. Yuan, Y.T. Zhu, Proc. Natl. Acad. Sci. USA 111 (2014) 7197–7201.
[18] Y.J. Wei, Y.Q. Li, L.C. Zhu, Y. Liu, X.Q. Lei, G. Wang, Y.X. Wu, Z.L. Mi, J.B. Liu, H. T. Wang, H.J. Gao, Nat. Commun. 5 (2014) 3580.
[19] K. Lu, Science 345 (2014) 1455–1456.
[20] X.L. Wu, F.P. Yuan, M.X. Yang, C.X. Zhang, P. Jiang, L. Chen, Y.G. Wei, E. Ma, Sci. Rep. 5 (2015) 11728.
[21] M.F. Ashby, in: G.S. Ansell (Ed.), Oxide Dispersion Strengthening, 431, Gordon and Breach, New York, 1968.
[22] J.F. Nie, Scr. Mater. 48 (2003) 1009–1015.
[23] J. da Costa Teixeira, L. Bourgeois, C.W. Sinclair, C.R. Hutchinson, Acta Mater. 57 (2009) 6075–6089.
[24] Y.N. Osetsky, D.J. Bacon, V. Mohles, Philos. Mag. 83 (2003) 3623–3641.
[25] Y.N. Osetsky, D.J. Bacon, Philos. Mag. 90 (2010) 945–961.
[26] C. Kohler, P. Kizler, S. Schmauder, Model. Simul. Mater. Sci. Eng. 13 (2005) 35–45.
[27] J.-H. Shim, D.-L. Kim, W.-S. Jung, Y.W. Cho, K.T. Hong, B.D. Wirth, J. Appl. Phys. 104 (2008) 083523.
[28] D. Terentyev, G. Bonny, L. Malerba, Acta Mater. 56 (2008) 3229–3235.
[29] D.J. Bacon, Y. Osetsky, D. Rodney, in: J.P. Hirth, L. Kubin (Eds.), Dislocations in Solids, 14, North-Holland, Amsterdam, 2009.
[30] Z.Z. Chen, N. Kioussis, Phys. Rev. B 80 (2009) 184104.
[31] C.V. Singh, D.H. Warner, Acta Mater. 58 (2010) 5797–5805.
[32] D. Terentyev, S.M.H. Haghighat, R. Schäublin, J. Appl. Phys. 107 (2010) 061806.
[33] D. Terentyev, G. Bonny, C. Domain, R.C. Pasianot, Phys. Rev. B 81 (2010) 214106.
[34] C.V. Singh, A.J. Mateos, D.H. Warner, Scr. Mater. 64 (2011) 398–401.
[35] Y. Mishin, D. Farkas, M.J. Mehl, Phys. Rev. B 59 (1999) 3393–3407.
[36] H. Tsuzuki, P.S. Branicio, J.P. Rino, Comput. Phys. Commun. 177 (2007) 518–523.
[37] R. Schwaiger, B. Moser, M. Dao, N. Chollacoop, S. Suresh, Acta Mater. 51 (2003) 5159–5172.
[38] Y.M. Wang, S. Cheng, Q.M. Wei, E. Ma, T.G. Nieh, A. Hamza, Scr. Mater. 51 (2004) 1023–1028.
[39] T.F. Dalla, P. Spatzig, R. Schaublin, M. Victoria, Acta Mater. 53 (2005) 2337–2349.
[40] T.R. Lee, C.P. Chang, P.W. Kao, Mater. Sci. Eng. A 408 (2005) 131–135.
[41] N. Krasilnikov, W. Lojkowski, Z. Pakiela, R. Valiev, Mater. Sci. Eng. A 397 (2005) 330–337.
[42] W.M. Yin, S.H. Whang, R.A. Mirshams, Acta Mater. 53 (2005) 383–392.
[43] C.D. Gu, J.S. Lian, Q. Jiang, Scr. Mater. 57 (2007) 233–236.